

Dark solitons and vortices in \mathcal{PT} -symmetric nonlinear media: from spontaneous symmetry breaking to nonlinear \mathcal{PT} phase transitions

V. Achilleos,¹ P.G. Kevrekidis,² D.J. Frantzeskakis,¹ and R. Carretero-González³

¹*Department of Physics, University of Athens, Panepistimiopolis, Zografos, Athens 157 84, Greece*

²*Department of Mathematics and Statistics, University of Massachusetts, Amherst, Massachusetts 01003-4515, USA*

³*Nonlinear Dynamical Systems Group, Computational Sciences Research Center,*

and Department of Mathematics and Statistics, San Diego State University, San Diego, CA 92182-7720, USA

We consider nonlinear analogues of Parity-Time (\mathcal{PT}) symmetric linear systems exhibiting defocusing nonlinearities. We study the ground state and excited states (dark solitons and vortices) of the system and report the following remarkable features. For relatively weak values of the parameter ε controlling the strength of the \mathcal{PT} -symmetric potential, excited states undergo (analytically tractable) spontaneous symmetry breaking; as ε is further increased, the ground state and first excited state, as well as branches of higher multi-soliton (multi-vortex) states, collide in pairs and disappear in blue-sky bifurcations, in a way which is strongly reminiscent of the linear \mathcal{PT} -phase transition —thus termed the nonlinear \mathcal{PT} -phase transition. Past this critical point, initialization of, e.g., the former ground state leads to spontaneously emerging solitons and vortices.

I. INTRODUCTION

Over the past decade, and since its original inception [1, 2], the theme of \mathcal{PT} -symmetric Hamiltonians has gained considerable momentum in the physics and applied mathematics communities. Such systems, respecting both Parity (\mathcal{P}) and Time-reversal (\mathcal{T}) symmetries —still exhibiting real spectra while non-Hermitian— provided an intriguing alternative to standard Hermitian quantum mechanics. Note that for a standard Schrödinger type Hamiltonian with a generally complex potential U , the \mathcal{PT} symmetry dictates that the potential satisfies the condition $U(x) = U^*(-x)$ [where $(\cdot)^*$ stands for complex conjugation].

Despite the theoretical appeal of such models, it was only recently shown [3] that optics could be an ideal playground for the physical/experimental realization of systems featuring the \mathcal{PT} symmetry. However, this also added another element in the interplay, namely nonlinearity. In that context, the considerations of Ref. [3] extended from bright and gap solitons to linear (Floquet-Bloch) eigenmodes in periodic potentials, examining how these coherent structures are affected by the genuinely complex, yet \mathcal{PT} -symmetric potentials. More recently, experimental results were reported both in nonlinear optical systems [4, 5] and electronic analogs thereof [6]. These, in turn, have triggered a wide range of theoretical studies on nonlinear lattices with either linear [7–15] or nonlinear [16–18] \mathcal{PT} -symmetric potentials and, more recently, on harmonic \mathcal{PT} -symmetric potentials [19].

While the above volume of work has examined numerous features extending from bright solitons to defect modes, and from gap solitons to \mathcal{PT} -lattices, the consideration of defocusing nonlinearities, and especially of dark solitons has been extremely limited (see, e.g., Ref. [20]). Little attention (and again chiefly in the focusing nonlinearity case [3]) has also been paid to \mathcal{PT} -symmetric systems in higher-dimensional settings and the corresponding interplay with nonlinear states such as vortices.

In the present work, we study systems with \mathcal{PT} -symmetric Hamiltonians exhibiting defocusing nonlinearities, and focus on the existence, stability and dynamical properties of the

ground state and excited states, i.e., dark solitons and vortices. Our main findings for a prototypical \mathcal{PT} -symmetric potential, which is harmonic in its real part and has a localized imaginary part (parametrized by an amplitude parameter ε) are summarized as follows: 1) dark solitons are shown to be subject to spontaneous symmetry-breaking (SSB) instabilities for small ε ; 2) for higher values of ε , the ground state and the first excited state (single dark soliton), as well as pairwise — e.g., 2nd and 3rd, 4th and 5th etc.— higher excited states (respective multiple dark soliton states) are subject to a nonlinear analogue of the \mathcal{PT} -phase transition, colliding and disappearing in a set of blue-sky bifurcations; 3) beyond this critical point, the system acts as a soliton generator, spontaneously emitting dark multi-soliton structures. 4) *All* of these features have direct counterparts for vortices in two-dimensional settings, illustrating the generic nature of these findings.

The paper is organized as follows. In Sec. II we introduce the model and study its one-dimensional (1D) version; in the same section, analytical and numerical results for the statics and dynamics of the ground state and dark solitons are presented; we also briefly touch upon the potential effects of noise in the gain profile. In Sec. III, we discuss nonlinear \mathcal{PT} -phase transitions occurring in the 1D setting and study the dynamics of the system beyond the relevant critical point. In Sec. IV, we generalize our findings in the two-dimensional (2D) setting, studying vortex states and their nonlinear \mathcal{PT} -phase transitions. Finally, in Sec. V, we present a summary of our results.

II. MODEL, GROUND STATE AND DARK SOLITONS

Our model, motivated by the above nonlinear optical considerations (but also by ones pertinent to nonlinear phenomena in Bose-Einstein condensates (BECs) [21]), will be, for the 1D setting, as follows:

$$i\partial_t u = -\frac{1}{2}\partial_x^2 u + |u|^2 u + [V(x) + iW(x)]u, \quad (1)$$

where u is the complex electric field envelope (or the macroscopic wavefunction in BECs), t denotes the propagation dis-

tance (or time in BECs) and x is the transverse direction. For a \mathcal{PT} -symmetric Hamiltonian, the real and imaginary parts of the potential must satisfy $V(x) = V(-x)$ and $W(x) = -W(-x)$. Below we focus on the case of a real parabolic potential

$$V(x) = \frac{1}{2}\Omega^2 x^2,$$

modeling the transverse distribution of the refractive index (or the external trap in BECs), while the imaginary part $W(x)$ is considered to be an odd, localized function of spatial width $\ll \Omega^{-1}$; as a prototypical example, we will consider

$$W(x) = \varepsilon x e^{-x^2/2}. \quad (2)$$

A generalization of this model in two-dimensions will be studied in Sec. IV.

Here, it is important to notice that the evolution of the power (number of atoms in BECs), $N = \int |u|^2 dx$, is governed by the equation

$$dN/dt = 2 \int |u|^2 W(x) dx. \quad (3)$$

Thus, since $W(x)$ is odd, if $|u|^2$ is even then N is conserved ($dN/dt = 0$). Below, we show that this is the case for the stationary states of the system that we will consider here, i.e., the ground state and excited states (dark solitons in 1D and vortices in 2D).

A. Ground state

We first analyze the most fundamental state, namely the ground state of the system, shown in Fig. 1. We seek stationary solutions of Eq. (1) in the form $u = u_b(x) \exp(-i\mu t)$, where μ is the propagation constant (or the chemical potential in BECs), while the background field u_b obeys the equation:

$$-\frac{1}{2}\partial_x^2 u_b + |u_b|^2 u_b + [V(x) + iW(x)]u_b - \mu u_b = 0. \quad (4)$$

For a sufficiently small imaginary potential, $W(x) = \varepsilon \tilde{W}(x)$ [with $\max\{|\tilde{W}(x)|\} = O(1)$], where $\varepsilon \ll 1$ [22], and when the inverse width Ω^{-1} of $V(x)$ is sufficiently large, $\Omega \sim \varepsilon$, we may find—in the Thomas-Fermi (TF) limit—an approximate solution of Eq. (1). This is of the form

$$u_b = [\sqrt{\mu} + f(x)] \exp[i\phi(x)], \quad (5)$$

where the amplitude and phase $f(x)$ and $\phi(x)$ (considered to be small, of order $\mathcal{O}(\varepsilon^2)$ and $\mathcal{O}(\varepsilon)$, respectively) are given by:

$$f(x) = -\frac{1}{2\sqrt{\mu}} (V + 2W^2), \quad \phi(x) = 2 \int \mathcal{W} dx. \quad (6)$$

where $\mathcal{W} = \int W dx$ (note that above integrals are indefinite ones). Contrary to the conservative case ($\varepsilon = 0$) [21], this TF background is characterized by a density dip located at

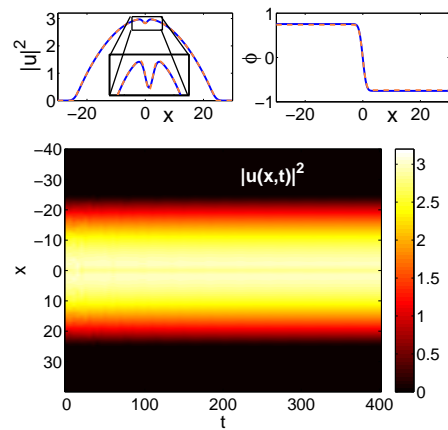


FIG. 1: (Color online) Top panels: density (left) and phase (right) of the numerically obtained TF background [solid (blue) line] compared to the prediction of Eqs. (6) [dashed (orange) line]; the inset shows the characteristic density dip induced by $W(x)$ at the origin. Bottom panel: contour plot showing the evolution of the density $|u(x,t)|^2$ with an initial condition $u(x,0) = u_b(x)$. Parameter values are: $\mu = 3$, $\Omega = 0.1$ and $\varepsilon = 0.4$.

the center ($x = 0$) and a nontrivial phase distribution. Both features are shown in the top panels of Fig. 1, where the analytical result is compared with the numerical one, which was obtained by means of a fixed-point algorithm (Newton's method). It is observed that the agreement between the two is excellent. Furthermore, a linear stability—Bogoliubov-de Gennes (BdG)—analysis (see, e.g., Ref. [23]) shows that the background $u_b(x)$ is stable against small perturbations.

The stability of the analytically found ground state solution has also been tested by means of direct numerical integration of Eq. (1) using as an initial condition Eq. (5), and it has been confirmed that it remains stable for long times, as shown in the bottom panel of Fig. 1. Note that this occurs even for relatively large ε (e.g., for $\varepsilon = 0.4$ used in the figure). As is observed, the ground state is practically stationary: it evolves in time only for a small initial time interval, during which the tails of the analytical solution slowly approach the ones of the exact ground state solution. This is expected because the spatial structure of the tails is different in the numerical and approximate solutions—due to the cutoff structure of the latter that becomes regularized—see, e.g., Ch. 6 of Ref. [24].

Beyond this initial transient (which is chiefly seeded by the tail and not the core of the wave form), the profile remains practically identical to the exact numerical solution in a wide spatial region—more than 90% of the TF radius $\sqrt{2\mu}/\Omega$; in fact, as we will show below, the relative error is of order of $\mathcal{O}(10^{-2})$ for $\varepsilon = \mathcal{O}(10^{-1})$. Thus, indeed, the error is of $\mathcal{O}(\varepsilon^2)$ and stays bounded within that order of approximation for extremely long evolution times; this indicates that, since the system under consideration possesses gain-loss, this state is indeed an attractor. This is, naturally, also the case at the vicinity of the central region where the imaginary potential $W(x)$ acts: our approximate solution for the ground state, Eqs. (5)-(6), predicts a localized dip in the density, with an approximation of the order $\mathcal{O}(\varepsilon^2)$.

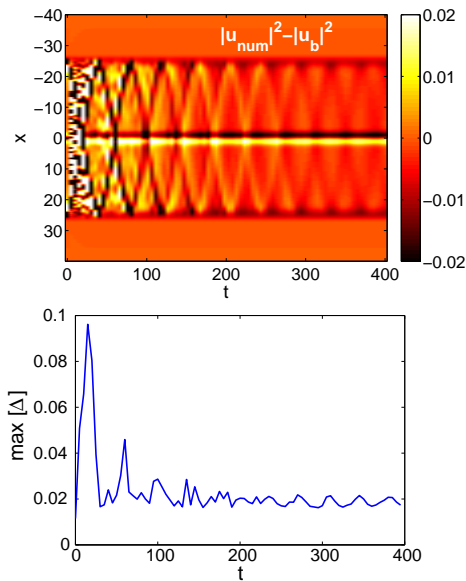


FIG. 2: (Color online) Top panel: contour plot showing the evolution of the density difference Δ [cf. Eq. 7] as a function of time. Bottom panel: the maximum value of Δ at the center. Parameter values are the same as the ones in Fig. 1.

The validity of the above arguments is clearly illustrated by the results shown in Fig. 2. In the top panel of this figure, we show a contour plot illustrating the time evolution of the density difference

$$\Delta(x, t) \equiv |u_{\text{num}}(x, t)|^2 - |u(x, t)|^2, \quad (7)$$

where $u(x, t)$ is the time evolution of the initial condition $u(x, 0) = u_b(x)$ (i.e., our approximate analytical solution for the ground state of the system), and $u_{\text{num}}(x)$ is the numerically found exact solution of the NLS Eq. (1). Since our approximation in deriving Eqs. (5)-(6) is valid up to order $\mathcal{O}(\varepsilon^2)$, the deviation from the “exact” (numerical) solution should be of order $\mathcal{O}(\varepsilon^2)$. As shown in the bottom panel of Fig. 2, this is the case indeed: the maximum of function Δ stays bounded by a constant prefactor (of order unity) times ε^2 .

B. Dark solitons

Apart from the ground state, excited states of the system—in the form of stationary dark solitons—can also be found numerically, by means of the Newton’s method. In particular, we decompose the field into the background u_b and the soliton $v(x, t)$, using the product ansatz:

$$\psi = u_b(x)v(x, t), \quad (8)$$

where the function $v(x, t)$ assumes—in the absence of the imaginary potential ($\varepsilon = 0$)—a hyperbolic tangent profile [23, 25]. Then, continuation in ε results in a dark soliton state, such as the one shown in the top panels of Fig. 3.

To describe analytically the dynamics of the dark soliton on top of the TF background, we substitute Eq. (8) into Eq. (1)

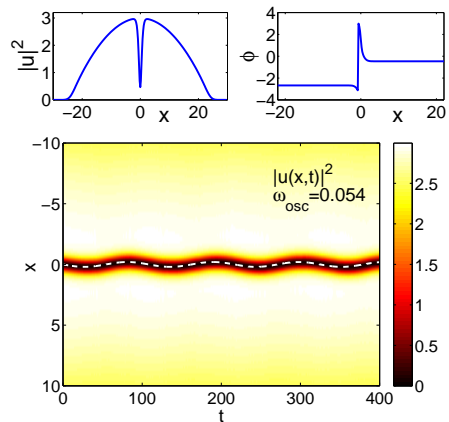


FIG. 3: (Color online) Top: density (left) and phase (right) of a single stationary dark soliton state. Parameters values are: $\mu = 3$, $\Omega = 0.1$ and $\varepsilon = 0.3$. Bottom: contour plot showing the small-amplitude oscillation of a dark soliton for $\varepsilon < \varepsilon_{cr}^{(1)}$. The dashed (white) line depicts the analytical result of Eq. (5). Parameters are as in the top panel, but for $\varepsilon = 0.04$.

and derive the equation:

$$i\partial_t v + \frac{1}{2}\partial_x^2 v - |u_b|^2 (|v|^2 - 1)v = -\partial_x \ln(u_b)\partial_x v. \quad (9)$$

Next, we substitute expressions (5)-(6) for u_b and simplify the resulting equation for $v(x, t)$ by Taylor expanding the right-hand side term as $\partial_x \ln(u_b) \approx \frac{1}{2}\partial_x f(1 + f + f^2 + \dots)$. Then, keeping only leading-order terms, up to order $\mathcal{O}(\varepsilon^2)$ [recall that the function $f(x)$ is of order $\mathcal{O}(\varepsilon^2)$], and using the scale transformations $t \rightarrow \mu t$ and $x \rightarrow \sqrt{\mu}x$, we obtain the following perturbed nonlinear Schrödinger (NLS) equation:

$$i\partial_t v + \frac{1}{2}\partial_x^2 v + v(1 - |v|^2) = \mu^{-2}P(v), \quad (10)$$

where the perturbation $P(v)$ is given by

$$P(v) = (1 - |v|^2)v (V + 2W^2) + v_x \left(\frac{1}{2}V_x - 2(W - i)W \right).$$

We now apply the perturbation theory for dark solitons (details can be found in the reviews [23, 25]). First we note that in the absence of the perturbation, $P(v) = 0$, Eq. (10) possesses a dark soliton solution of the form:

$$v(x, t) = \cos \varphi \tanh \xi + i \sin \varphi, \quad (11)$$

where $\xi \equiv \cos \varphi [x - x_0(t)]$, with φ and $x_0 = (\sin \varphi)t$ representing the soliton phase angle and center of the soliton, respectively. Then, in the case $P(v) \neq 0$, and in the framework of the adiabatic approximation, the functional form of the soliton of Eq. (10) is assumed to be unchanged, but its parameters φ and x_0 become unknown slowly-varying functions of time. We find that the evolution of these parameters, which is determined by the perturbation-induced change of the energy of

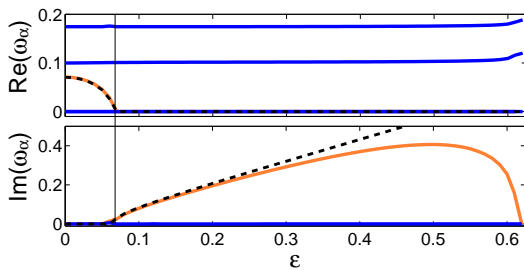


FIG. 4: (Color online) The linear spectrum, as obtained numerically by the BdG analysis, of the single dark soliton branch for $\Omega = 0.1$ and $\mu = 3$: top (bottom) panel shows the real (imaginary) part of the lowest eigenfrequencies ω as a function of the amplitude ε . The lowest solid (orange) line in the top panel and the upper solid (orange) curve in the bottom panel depict, respectively, the real and imaginary part of the anomalous mode eigenfrequency ω_α . The dashed (black) lines in both panels indicate the analytical result of Eq. (14). The thin vertical line shows the point $\varepsilon_{cr}^{(1)}$, where the anomalous mode eigenfrequency becomes imaginary.

the system [23, 25], is described by the following equations:

$$\frac{dx_0}{dt} = \sin \varphi(t), \quad (12)$$

$$\frac{d\varphi}{dt} = -\frac{1}{2}\partial_x V - \int \text{sech}^4(\xi) [\tanh(\xi)W^2 + WW] dx, \quad (13)$$

where we have assumed almost black solitons, with sufficiently small phase angles. This way, we can combine Eqs. (12) and (13) and derive, for a given $W(x)$, an equation of motion for the soliton center x_0 . Hereafter, we specify a Gaussian-shaped imaginary potential of the form (2). Note that other choices, e.g., $W(x) = \varepsilon \text{sech}^2(x) \tanh(x)$, have led to similar results. To examine the stability of the equilibrium at $x_0 = 0$, we Taylor expand Eq. (13), obtaining to leading order

$$\frac{d^2 x_0}{dt^2} = -\omega_{\text{osc}}^2 x_0, \quad \omega_{\text{osc}}^2 \approx \left(\frac{\Omega}{\sqrt{2}}\right)^2 - \frac{6}{5}\varepsilon^2. \quad (14)$$

Equation (14) implies that if the amplitude ε of $W(x)$ is less than a critical value, $\varepsilon_{cr}^{(1)} = \sqrt{5/12}\Omega$, then the soliton performs oscillations in the complex potential with frequency ω_{osc} . Such a case is demonstrated in the bottom panel of Fig. 3, where we show a dark soliton oscillating around the trap center for $\varepsilon = 0.04 < \varepsilon_{cr}^{(1)}$. The numerically found trajectory, obtained by direct numerical integration of Eq. (1), is compared with the analytical result of Eq. (14) [dashed (white) line]; as is observed, the agreement between the two is excellent.

On the other hand, Eq. (14) dictates that if $\varepsilon > \varepsilon_{cr}^{(1)}$ then the soliton will become unstable. The above prediction has been confirmed numerically, both by means of direct simulations and by employing a BdG analysis. In the framework of the latter, the stability of the dark soliton is studied by considering the anomalous mode eigenfrequency ω_α (which is

associated with the dark soliton motion [23, 26]). If the imaginary part of this eigenfrequency is zero (nonzero) then the soliton is stable (unstable). We have found that this eigenfrequency is real for $\varepsilon < \varepsilon_{cr}^{(1)}$ and, in this case, ω_α coincides with the analytically found oscillation frequency ω_{osc} . On the other hand, for values $\varepsilon > \varepsilon_{cr}^{(1)}$, the anomalous mode eigenfrequency ω_α becomes imaginary, thus signaling the onset of the spontaneous symmetry-breaking (SSB) instability of the dark soliton, which displaces the dark soliton from the trap center. The detailed dependence of ω_α on the amplitude ε of the imaginary potential W , as found by the BdG analysis, is illustrated in Fig. 4. It is observed that the anomalous mode ω_α initially moves towards the origin, and past the critical point $\varepsilon_{cr}^{(1)}$ (cf. thin vertical line), becomes imaginary, manifesting the soliton's exponential instability. Importantly, as shown in Fig. 4, for small ε the agreement between the analytical prediction of Eq. (14) [dashed (black) line] and the BdG numerical result [lowest solid (orange) line] is excellent.

C. Effect of noise-induced perturbations

Let us now consider an experimentally relevant situation, where the (localized) gain which acts on the system is associated with the presence of noise. This is important in order to ensure the robustness of our results presented above in realistic cases where \mathcal{PT} -symmetry is not strictly enforced. In such a case, an important question is if and how the noise-induced perturbation affects the stability and dynamics of the ground state and the dark soliton. To address this question, we assume that—in the simplest approximation—the gain side of the potential $W(x)$ (for $x > 0$) now becomes $W(x)[1 + \delta n(x)]$; here, $n(x)$ is a uniformly distributed noise of amplitude δ . Thus, generally, one expects from Eq. (3) that since the noise $n(x)$ is not parity symmetric, $dN/dt \neq 0$, i.e., for any time instant t , the system will either grow ($dN/dt > 0$) or decay ($dN/dt < 0$). As a result, stationary states (such as the TF background ground state or a single- or multiple-dark-soliton state) cannot generically exist, at least in the case of relatively large noise amplitude.

To investigate the significance of this effect of noise, we have numerically integrated Eq. (1) with prototypical initial conditions of relevance to our study including the TF background and the dark soliton, and have let the system to evolve in the presence of noise perturbations. The results of our simulations can be summarized in the examples shown in Fig. 5, where contour plots showing the evolution of the density of the TF background (top panels) and a single dark soliton (bottom panels) are given. It is observed that if the noise amplitude δ is sufficiently small (the value $\delta = 0.1$ was used in the left panels of the figure) then the dynamics is practically unaffected by the effect of noise (in fact, the effect of noise can be observed for larger values of δ , as is explained below). Note that in the case of the dark soliton, the noise induces the soliton to perform small-amplitude oscillations (cf. inset in the bottom left panel of Fig. 5) which can be very well described by Eq. (14). On the other hand, if the noise is strong enough

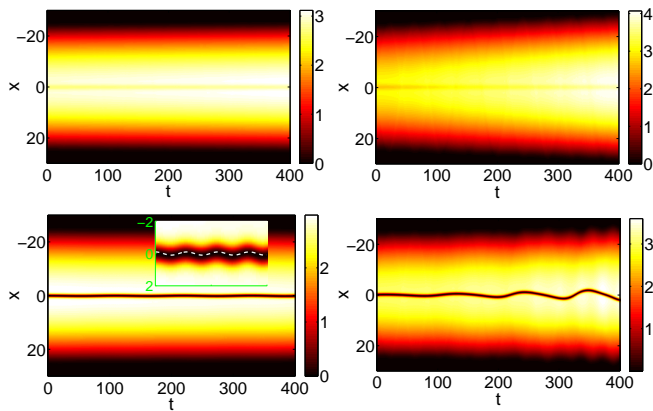


FIG. 5: (Color online) Contour plots, showing the evolution of the density when noise is added to Eq. (1), on the gain side of the imaginary potential ($x > 0$). Top: for a relatively small amplitude noise, $\delta = 0.1$, the TF background evolves practically unaffected [left], while for a larger noise, $\delta = 1$ the background grows [right]. In both top panels $\varepsilon = 0.4$. Bottom: a dark soliton, performs small amplitude oscillations (see inset) after perturbed by a small amplitude noise of $\delta = 0.1$ [left], while a dark soliton is oscillating with a growing amplitude for a larger amplitude noise, $\delta = 1$ [right]. The amplitude of the imaginary potential is $\varepsilon = 0.04$, for both panels, where in the absence of noise the soliton is stable [cf. Fig. (4)]. Other parameter values are: $\mu = 3$, $\Omega = 0.1$.

(as, e.g., with $\delta = 1$ used in the right panels) then the ground state either grows or decays, depending on the initial sign of dN/dt (which depends, in turn, on the particular noise realization), with an average growth rate determined by the parameter δ . Notice that, in this case of large-amplitude noise, the dark soliton becomes thermodynamically unstable and is displaced from the center, performing oscillations of growing amplitude. The approximate evolution equation for the dark soliton, Eq. (14), is not valid here, since the noise term becomes of the same order ε as the rest of the perturbation and needs to be explicitly accounted for in the anti-damped dynamics of the solitary wave.

Overall, these results support that under weak noise perturbations, the phenomenology presented above (and below) will persist. Yet, for strong random perturbations, the phenomenology changes considerably and should be considered separately in further detail.

III. NONLINEAR \mathcal{PT} PHASE TRANSITIONS

Let us now return to the results of the BdG analysis presented in the previous section, and discuss in more detail what happens beyond the SSB instability of the single dark soliton state. As shown in Fig. 4, for values of $\varepsilon > \varepsilon_{cr}^{(1)}$ the unstable imaginary eigenvalue makes a maximal excursion along the imaginary line and returns to the origin at a second critical point, $\varepsilon_{cr}^{(2)} = 0.62$, finally colliding with it. The branch of single soliton solutions disappears past this critical point. To better understand how the branch ceases to exist, we first observe (see top panel of Fig. 3) that the density profile of the

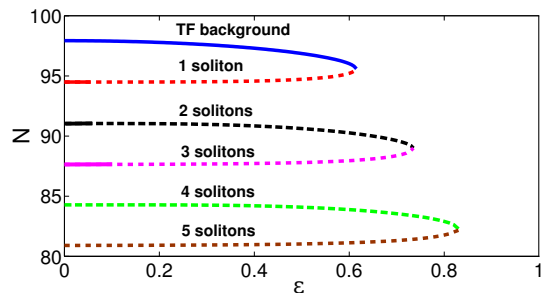


FIG. 6: (Color online) The power N as function of the strength ε of the imaginary potential, depicting the full bifurcation diagram for the ground state and excited states in 1D. The diagram encompasses the pairwise blue-sky bifurcations/disappearances of the nonlinear states, namely the ground state with the 1st excited state (single dark soliton), the 2nd with the 3rd excited state (two- and three-dark-solitons), the 4th with the 5th, and so on. Solid (dashed) lines indicate dynamically stable (unstable) branches. Here, $\mu = 3$ and $\Omega = 0.1$.

soliton becomes increasingly shallower (i.e., more “grey”) as ε grows and the second critical point is approached. This is due to the development of an increasingly strong *even* imaginary part of the solution. Furthermore, the stable background (ground state) solution $u_b(x)$ [cf. Eqs. (5)-(6) and top panel of Fig. 1] develops an *odd* imaginary part resembling a (progressively darker) grey soliton. Finally, at $\varepsilon = \varepsilon_{cr}^{(2)}$, the profiles of these modes become identical and disappear in a blue-sky bifurcation through their collision. This is shown in Fig. 6, where the power N is shown as a function of ε . The top solid (blue) branch shows the stable ground state, u_b , which ultimately collides with the one soliton (first excited) state at $\varepsilon \approx 0.62$ (for $\mu = 3$ and $\Omega = 0.1$).

Importantly, we have confirmed that the above description holds also for higher excited states (multiple dark soliton solutions), as shown in Fig. 6: each pair of the higher excited states (2nd with 3rd, 4th with 5th, etc.) also disappears in a blue-sky bifurcation. A general remark is that higher excited states bifurcate for larger values of ε . Remarkably, this can be thought of as a *nonlinear analogue* of the \mathcal{PT} transition, in analogy with the pairwise collisions in Ref. [1] (see, e.g., Fig. 1 of that reference) for the linear setting [27].

A relevant and interesting question concerns the dynamics of the nonlinear states when subject to these (SSB and blue-sky) bifurcations. To answer this, we numerically integrated Eq. (1) and the relevant results are shown in Fig. 7. In the top panels, we illustrate the dynamics of the dark soliton upon its destabilization at $\varepsilon = \varepsilon_{cr}^{(1)}$. When the SSB is manifested, the soliton is either spontaneously ejected towards the lossy side (and typically found to localize therein, while the background grows in amplitude and widens) or moves to the gain side, executing oscillations thereafter.

On the other hand, past $\varepsilon = \varepsilon_{cr}^{(2)}$, using, as an initial condition the form of the TF background (bottom panels of Fig. 7), we have found that a dark soliton train is spontaneously formed, with an increasingly larger number of solitons as larger values of ε are used. This can be intuitively connected to the observation of Fig. 7 that higher excited multi-

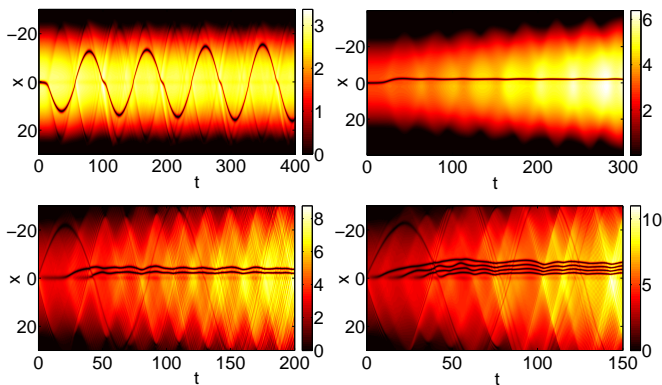


FIG. 7: (Color online) Bifurcation-induced dynamics. Top panels: manifestations of the SSB destabilization scenarios for an unstable dark soliton past $\varepsilon = \varepsilon_{cr}^{(1)}$. Bottom panels: soliton generator, spontaneously leading to two or four solitons from the ground state used for $\varepsilon > \varepsilon_{cr}^{(2)}$. The parameters are $\mu = 3$ and $\Omega = 0.1$ and $\varepsilon = 0.3$ (top row), $\varepsilon = 0.64$ (bottom left), and $\varepsilon = 0.7$ (bottom right).

soliton states persist for larger ε than lower ones. Again, it is typically observed that the solitons are nucleated and stay in the vicinity of the global minimum of $W(x)$, which corresponds to the “lossy” side of the imaginary potential.

IV. TWO-DIMENSIONAL GENERALIZATIONS

Finally, we consider the case of a 2D \mathcal{PT} -symmetric potential with a real parabolic part

$$V(x, y) = \frac{1}{2}\Omega^2(x^2 + y^2),$$

and an odd [$W(-x, -y) = -W(x, y)$] imaginary part

$$W(x, y) = \varepsilon(x + y)e^{-(x^2 + y^2)/4}.$$

The bifurcation of the nonlinear structures emerging in 2D follows a similar, but also more complex, pattern than in the corresponding 1D setting. Figure 8 depicts the full bifurcation scenario for solutions bearing no vortices (the TF background cloud), one to six vortices, and the dark soliton stripe. As in 1D, the TF background is stable in all its domain of existence and collides, in a blue-sky bifurcation, for a large enough value of ε , with an excited state. However, in contrast to the 1D case where this collision happens with the *second* excited state, in 2D the collision occurs with the *second* excited state, due to the absence of net topological charge in such a vortex-dipole (see top-right red curve) bearing two opposite charge vortices emerging from the central dip of the TF background. At this critical point $\varepsilon = \varepsilon_{cr}^{(2)}$ the dipole branch is unstable, having been destabilized through an SSB bifurcation at an $\varepsilon = \varepsilon_{cr}^{(1)} > 0$ value (below which for $\varepsilon > 0$ the dipole is stable—see portion of red solid line in the figure). As this branch is followed (from top to bottom in the figure), a series of bifurcations occur where the existing vortices are

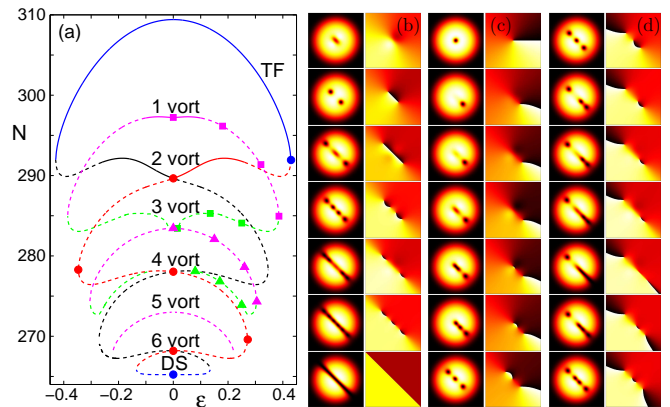


FIG. 8: (Color online) The 2D generalization. (a) Bifurcation diagram for the 2D stationary nonlinear (vortex and DS stripe) states. Stable (unstable) branches, as per the corresponding BdG analysis, are depicted with solid (dashed) lines. (b) Series of density (left) and phase (right) configurations along the branch with even number of vortices corresponding to the circles in panel (a) [from top to bottom]. (c) Same as (b) for the branch starting with one vortex and connecting with three vortices corresponding to the squares in panel (a) [from top to bottom]. (d) Same as (b) for the branch starting with three symmetric vortices and ending with four vortices corresponding to the triangles in panel (a) [from top to bottom]. Parameter values are: $\mu = 2$ and $\Omega = 0.2$. The field of view for the configurations is $[-10.5, 10.5] \times [-10.5, 10.5]$.

drawn to the periphery of the cloud, a dip in the center deepens leading eventually to a new vortex pair emerging (i.e., a higher excited state). In this manner the branches with *even* number of vortices are all connected. As more and more vortex pairs emerge, the cloud “saturates” and can no longer fit in new vortex pairs finally colliding with a dark soliton stripe (see lower blue branch in the figure). This overall bifurcating structure of even vortices—with a $\varepsilon \rightarrow -\varepsilon$ symmetry where the solutions are just flipped by $(x, y) \rightarrow (-x, -y)$ —is depicted, with density and phase profiles, in the series of panels of Fig. 8(b).

As for the bifurcation scenario of *odd* number of vortices, the first excited state bearing a single vortex at the origin (for $\varepsilon = 0$) is stable for small values of ε , while it again sustains an SSB bifurcation for larger ε . As ε increases the vortex moves towards the periphery of the cloud and a dip at the center of the cloud deepens until a vortex pair emerges from it. This scenario connects the one-vortex branch with the *asymmetric* three-vortex (+ − + vortex tripole) branch, as it is depicted with the top (magenta and green) lines in panel 8(a) and the series of snapshots in panels 8(c). As it is evident from the figure, the asymmetric three-vortex branch eventually connects with the symmetric one for values of $\varepsilon \rightarrow 0$. A similar bifurcation occurs with the symmetric three-vortex branch, which becomes asymmetric with a deepening dip at the center where a vortex pair emerges (at the same time that a vortex is lost at the periphery), connecting in this way with the four-vortex branch [see series of snapshots in panels 8(d)].

As for the dynamics of unstable steady states, we have observed—in analogy with the 1D case—that (a) a single vortex

tends to migrate towards the minimum of the lossy side of the potential, while the remaining vortices (if present) perform almost circular orbits at the periphery of the cloud where they are eventually absorbed; and (b) past $\varepsilon = \varepsilon_{cr}^{(2)}$, using as an initial condition the form of the TF background, also produces the spontaneous formation of an increasing number of vortices for larger values of ε (namely, a “vortex generator”). It is worth mentioning that the precise structure of the bifurcation diagram depends of the values of the propagation constant μ and the trap strength Ω . For weaker Ω and/or larger μ the extent of the TF background will be larger allowing for a longer bifurcating chain of higher-order vortex states. Nonetheless, the displayed SSB instabilities and phenomenology and the nonlinear \mathcal{PT} transition involving the cascade of blue-sky bifurcations (notice that in the 2D case the order is reversed and the largest ε bifurcation is that involving the TF and the dipole states) appear to be universal in confining \mathcal{PT} -symmetric potentials.

V. CONCLUSIONS

In the present work, we have developed some fundamental insights stemming from the interplay of defocusing nonlinearity and \mathcal{PT} -symmetric confining potentials. We identified both a symmetry-breaking bifurcation destabilizing the dark solitons that leads to non-stationary dynamics, as well as a nonlinear analogue of the \mathcal{PT} transition that eventually terminates both the ground state and the dark soliton branch, yielding purely gain-loss dynamics within the system. Similar bifurcation phenomena and dynamics of mobility or of spon-

taneous emergence of dynamical patterns forming out of the destabilization of the nonlinear states were identified in two-dimensional settings, for vortices.

These investigations, we believe, pave the way for studying \mathcal{PT} -symmetric systems in the context of defocusing nonlinearities and of higher dimensional systems, which are some of the natural extensions of the \mathcal{PT} -symmetric literature. A canonical set of investigations which is still missing concerns the effects of such potentials in three-dimensional continuum or higher dimensional lattice contexts, as well as the manipulation of nonlinear states emerging in these systems. Another relevant possibility arising from our considerations here in is the study of inexact \mathcal{PT} -symmetric nonlinear systems and their comparison to exact ones, as well as the consideration of the interplay of the nonlinearity with merely loss (rather than gain-loss) in the passive- \mathcal{PT} nonlinear settings. These themes will be pursued in future works.

Acknowledgments

The work of D.J.F. was partially supported by the Special Account for Research Grants of the University of Athens. P.G.K. gratefully acknowledges support from the National Science Foundation under grants DMS-0806762 and CMMI-1000337, as well as from the Alexander von Humboldt Foundation, the Alexander S. Onassis Public Benefit Foundation and the Binational Science Foundation. R.C.G. gratefully acknowledges support from the National Science Foundation under grant DMS-0806762.

-
- [1] C.M. Bender and S. Boettcher, Phys. Rev. Lett. **80**, 5243 (1998).
 - [2] C.M. Bender, S. Boettcher, and P.N. Meisinger, J. Math. Phys. **40**, 2201 (1999); C.M. Bender, Rep. Prog. Phys. **70**, 947 (2007).
 - [3] Z. H. Musslimani, K. G. Makris, R. El-Ganainy, and D. N. Christodoulides, Phys. Rev. Lett. **100**, 030402 (2008); K.G. Makris, R. El-Ganainy, D.N. Christodoulides and Z.H. Musslimani, Phys. Rev. A **81**, 063807 (2010).
 - [4] A. Guo, G. J. Salamo, D. Duchesne, R. Morandotti, M. Volatier-Ravat, V. Aimez, G. A. Siviloglou and D. N. Christodoulides, Phys. Rev. Lett. **103**, 093902 (2009).
 - [5] C.E. Rüter, K.G. Makris, R. El-Ganainy, D.N. Christodoulides, M. Segev, D. Kip, Nature Phys. **6**, 192 (2010).
 - [6] J. Schindler, A. Li, M.C. Zheng, F.M. Ellis and T. Kottos, Phys. Rev. A **84**, 040101 (2011).
 - [7] H. Ramezani, T. Kottos, R. El-Ganainy and D.N. Christodoulides, Phys. Rev. A **82**, 043803 (2010).
 - [8] A.A. Sukhorukov, Z. Xu and Yu.S. Kivshar, Phys. Rev. A **82**, 043818 (2010).
 - [9] M.C. Zheng, D.N. Christodoulides, R. Fleischmann and T. Kottos, Phys. Rev. A **82**, 010103(R) (2010).
 - [10] E.M. Graefe, H.J. Korsch and A.E. Niederle, Phys. Rev. Lett. **101**, 150408 (2008).
 - [11] E.M. Graefe, H.J. Korsch and A.E. Niederle, Phys. Rev. A **82**, 013629 (2010).
 - [12] Z. Lin, H. Ramezani, T. Eichelkraut, T. Kottos, H. Cao and D.N. Christodoulides, Phys. Rev. Lett. **106**, 213901 (2011).
 - [13] K. Li and P. G. Kevrekidis, Phys. Rev. E **83**, 066608 (2011).
 - [14] S. V. Dmitriev, S. V. Suchkov, A. A. Sukhorukov, and Yu.S. Kivshar, Phys. Rev. A **84**, 013833 (2011).
 - [15] S. V. Suchkov, B. A. Malomed, S. V. Dmitriev and Yu.S. Kivshar, Phys. Rev. E **84**, 046609 (2011).
 - [16] A.E. Miroshnichenko, B.A. Malomed, and Yu.S. Kivshar Phys. Rev. A **84**, 012123 (2011).
 - [17] F. Kh. Abdullaev, Y. V. Kartashov, V. V. Konotop and D. A. Zezyulin, Phys. Rev. A **83**, 041805 (2011).
 - [18] D. A. Zezyulin, Y. V. Kartashov, V. V. Konotop, Europhys. Lett. **96**, 64003 (2011).
 - [19] D. A. Zezyulin and V. V. Konotop, arXiv:1201.6638.
 - [20] H. G. Li, Z. W. Shi, X. J. Jiang, and X. Zhu, Opt. Lett. **36**, 3290 (2011).
 - [21] P.G. Kevrekidis, D.J. Frantzeskakis, and R. Carretero-González, *Emergent Nonlinear Phenomena in Bose-Einstein Condensates: Theory and Experiment* (Springer-Verlag, Heidelberg, 2008).
 - [22] Note that ε is measured in units of the free space wavelength (in optics) or in units of energy (in BECs).
 - [23] D.J. Frantzeskakis, J. Phys. A: Math. Theor. **43**, 213001 (2010).
 - [24] C. J. Pethick and H. Smith, *Bose-Einstein condensation in dilute gases* (Cambridge University Press, Cambridge, 2002).
 - [25] Yu.S. Kivshar and B. Luther-Davies Phys. Rep. **298**, 81 (1998).

- [26] G. Theocharis, P.G. Kevrekidis, M.K. Oberthaler, and D.J. Frantzeskakis Phys. Rev. A 76, 045601 (2007); G. Theocharis, A. Weller, J.P. Ronzheimer, C. Gross, M.K. Oberthaler, P.G. Kevrekidis, and D.J. Frantzeskakis Phys. Rev. A **81**, 063604 (2010).
- [27] Despite the similarity of the two figures, it does not escape us

that an interesting difference exists: in the linear picture the lowest eigenvalues collide the last, while in the 1D nonlinear case the lowest eigenstates disappear the first, a feature that important consequences for the supercritical dynamics of Fig. 6.